

Multi-scale modular analysis of open volumetric receivers for central tower CSP systems

Original

Multi-scale modular analysis of open volumetric receivers for central tower CSP systems / Cagnoli, Mattia; Froio, Antonio; Savoldi, Laura; Zanino, Roberto. - In: SOLAR ENERGY. - ISSN 0038-092X. - ELETTRONICO. - 190:(2019), pp. 195-211. [10.1016/j.solener.2019.07.076]

Availability:

This version is available at: 11583/2748312 since: 2019-08-22T13:18:03Z

Publisher:

Elsevier

Published

DOI:10.1016/j.solener.2019.07.076

Terms of use:

This article is made available under terms and conditions as specified in the corresponding bibliographic description in the repository

Publisher copyright

Elsevier postprint/Author's Accepted Manuscript

© 2019. This manuscript version is made available under the CC-BY-NC-ND 4.0 license
<http://creativecommons.org/licenses/by-nc-nd/4.0/>. The final authenticated version is available online at:
<http://dx.doi.org/10.1016/j.solener.2019.07.076>

(Article begins on next page)

Multi-scale modular analysis of open volumetric receivers for central tower CSP systems

Mattia Cagnoli ¹, Antonio Froio ¹, Laura Savoldi ^{1,*}, Roberto Zanino ¹

¹ *Dipartimento Energia, Politecnico di Torino, Corso Duca degli Abruzzi 24, 10129 Torino, Italy*

*corresponding author: laura.savoldi@polito.it

Abstract

Open volumetric air receivers (OVARs) are an interesting Concentrating Solar Power (CSP) technology, due to the high temperature that can be reached by the heat transfer fluid (air at ambient pressure), leading to high efficiency of the power cycle.

In this paper, a novel multiscale and modular computational approach is proposed and applied to the analysis of a conventional OVAR, consisting of several honeycomb cups, each including a large number of parallel prismatic channels. The methodology proposed in this work consists in scaling-up the receiver numerical model, from the single channel (micro-scale), through the cup (meso-scale), to the whole receiver (macro-scale), exploiting the results obtained at the micro-scale to characterize the model applicable at the meso-scale, which is then used to modularly generate the model at the macro-scale. The rationale of the multi-scale approach is to take into account at each scale the most relevant phenomena that affect the receiver performance at that scale, which cannot be considered in detail at larger scales. Starting from the thermal-hydraulic characterization at the micro-scale, obtained by means of a detailed 3D CFD model of the generic (single) channel, the meso-scale problem is addressed introducing an equivalent 1D porous medium model for the generic cup, implemented in the Modelica environment. The latter model is finally exploited to assemble a macro-scale model able to describe the entire receiver behavior, considering also the return air flow that laps the lateral walls of the cups.

The receiver macro-scale model has been preliminarily compared with the data collected during the SolAir 200 experimental campaign, conducted at the PSA in the early 2000s, demonstrating that the model developed here provides credible results. A first application of the developed multi-scale model is also presented, in order to demonstrate the potential of this approach. The results from this analysis are discussed, underlining the influence of the phenomena that affect the receiver performance at the different scales. Particularly, the effect of the return air flow is investigated, as well as the effect of a non-uniform solar heat flux distribution. In the latter case, the model has been used to calibrate the opening of the orifices installed at the cup rear side to regulate the mass flow rate among the cups forcing an almost uniform air outlet temperature. Moreover, the full receiver model is applied to a simple transient scenario consisting of a fast passing cloud, proving the ability of the model to simulate dynamic conditions in a reasonable way.

Keywords: CSP, central tower systems, open volumetric receiver, multiscale approach, CFD, Modelica

Nomenclature			
A	Area	Abbreviations	
A_L	Heat transfer area between the cup and the air return (gap) flow model	ARR	Air Return Ratio
d	Channel depth	CFD	Computational Fluid Dynamic
D_{eq}	Hydraulic diameter	CSP	Concentrated Solar Power
f	Friction factor	CV	Control Volume
F	View factor	HTC	Heat Transfer Coefficient
h	Specific enthalpy	OVAR	Open Volumetric Air Receiver
H	Heat transfer coefficient	SiC	Silicon Carbide
J	Inertial coefficient	SiSiC	Siliconized Silicon Carbide
k	Thermal conductivity	Subscripts	
K	Permeability	abs	Absorbed
L	Channel aperture size	amb	Ambient
\dot{m}	Mass flow rate	AR	Air return (gap) model
Nu	Nusselt number	bulk	At the fluid bulk
p	Pressure	c	Selective coating
Re	Reynolds number	cond	Thermal conduction
t	Time	conv	Convective
T	Temperature	ext	External
u	Air speed (fluid volume)	f	Fluid
V	Volume	fm	Mean fluid temperature in the CV
w	Channel wall thickness	front	Front face
z	Distance along the channel axis from the channel inlet	i	i-th control volume
Greek symbols		in	Inlet / Incident
Δz	Length of the discretization interval	j	Cup j-th control volume (in the air return model)
Δp	Pressure drop	k	Square root of permeability used as characteristic length
ε	Emissivity	loss	Heat losses
η	Efficiency	out	Outlet
μ	Dynamic viscosity	rad	Radiative
ρ	Density	rec	Receiver
φ	Porosity	return	Return air
σ	Stefan–Boltzmann constant	s	Solid
$\dot{\phi}$	Heat flux	sol	Solar
ϕ	Thermal power	v	Per unit volume
Φ_{vol}	Volumetric heat source	wall	At the wall
		x	x-th cup in the receiver
		z	Along the channel axis

1 Introduction

The environmental impact linked with the fossil fuel consumption imposes to rethink the way to produce electricity. Renewable sources will certainly play a key role in the future energy scenario; particularly solar energy, which is an extremely abundant resource exceeding several times the current energy demand (Abbott, 2010).

Concentrated Solar Power (CSP) can be considered an advantageous technology to exploit the solar energy, producing dispatchable heat and power. However, CSP is still not competitive in terms of costs with respect to the convectional fossil-fuel power plants, although a sharp cost reduction has been observed in the last years (IRENA, 2018). To overcome this economic gap, the solar-to-electricity efficiency needs to be improved. This goal can be achieved, according to Carnot's theorem, increasing the temperature of the heat source that drives the thermodynamic power cycle, i.e. the temperature of the heat transfer fluid that leaves the receiver. In this context, central tower systems using volumetric receivers are an interesting technology due to the high operating temperature that can be reached by the

gaseous heat transfer fluid, which in theory could reach up to 1500°C using ceramic absorbers (Ho and Iverson, 2014), even if more realistic temperatures are not higher than 1000 °C due to the material oxidation in the long term.. The OVAR technology, with ceramic absorber, has been widely investigated in past projects (Hoffschmidt et al., 2003; Téllez, 2003; Téllez et al., 2004). Thermal efficiencies reached during these experimental campaigns range from 70% to 83% with the air outlet temperature between 700 °C and 800 °C, respectively (Ávila-Marín, 2011). To demonstrate the maturity of the open-loop volumetric receiver technology, a pilot plant was built in Jülich, Germany (Hennecke et al., 2007).

The peculiarity of the volumetric receiver is that the solar radiation penetrates deeply inside the porous medium heating the solid structure, as opposed to the more common external tubes receiver, where only the outer tubes surface is exposed to the concentrated sun light. The absorber structure is cooled by an air stream that flows through the porous volume lapping directly the irradiated surfaces. The deep penetration of the solar radiation in the absorber structure may result in the so-called volumetric effect, which occurs when the irradiated front face of the receiver is colder than the outlet air temperature (Ávila-Marín, 2011). For a given outlet fluid temperature, the occurrence of the volumetric effect helps to reduce the convective and radiative heat losses towards the environment. However, the volumetric effect has never been achieved in the receivers tested to date (Kribus et al., 2014), at least considering large-scale experiments on receivers based on a standard honeycomb structure.

The present paper focuses on the open volumetric configuration, which exploits atmospheric air at ambient pressure. A conventional OVAR has a modular, multi-scale structure. As shown in Figure 1, the receiver consists of several cups, each including a large number of parallel prismatic channels and resulting in a well-ordered (honeycomb) porous structure. Both metals and ceramics have been used as materials for the porous structure; however, ceramics are obviously more suitable if very high air temperatures are to be reached. Adjacent cups are separated by a gap, which is exploited to lead the return air from the power conversion unit back to the irradiated receiver face, in order to cool the supporting structure and preheat the inlet ambient air. The share of the return air that is actually recirculated in the porous absorber structure defines the air return ratio (ARR).

Marcos et al. (2004) investigated different solutions to enhance the air return ratio on the base of a Computational Fluid Dynamic (CFD) comparative analysis considering different receiver configurations. Marcos proposed a change in the cup shape consisting in the smoothing of the edges of the irradiated face, as it can be seen in Figure 1b. Stadler et al. (2017) experimentally studied the influence of an external air return system on the receiver performance at the Jülich solar tower plant.

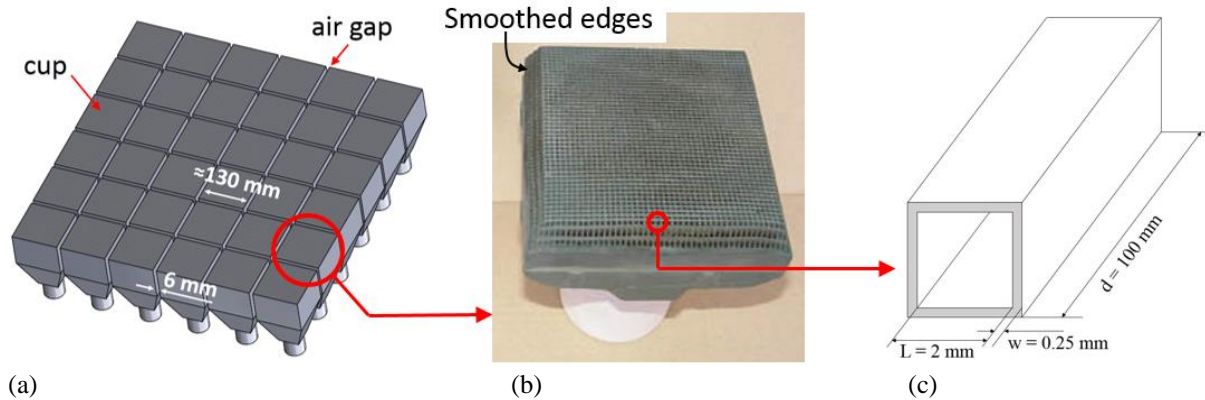


Figure 1 – Zooming-in from the entire receiver (a), to the cup (Stobbe Tech A/S, 2017) (b), and finally to the single channel (c). The considered size of the cup, of the single channel and of the air gap that separates the adjacent cups are also provided.

In addition to experimental studies, numerical models have been proposed in the literature to simulate the thermal-hydraulic behavior of open volumetric receivers. The interest in the numerical modeling of such kind of receivers is linked with the possibility to explore a wide range of geometric and thermodynamic parameters of the absorber structure, looking for an optimized configuration able to significantly improve the receiver performance. According to Capuano et al. (2016), two approaches have been adopted so far:

- the so-called discrete method, which focuses on the detailed thermal-hydraulic analysis of a small portion of the absorber structure (e.g., a single channel in the case of honeycomb structures). This methodology

considers the actual absorber geometry and it was proved to be reliable (Fend et al., 2013); however, it cannot be used to simulate the entire receiver.

- the continuum representation of the absorber structure. Contrary to the discrete representation, in the continuum approach the whole absorber is simulated as a porous continuum described by effective homogenized properties. The low computational cost of this approach is compensated by the fact that the details of the absorber structure cannot be included in the model.

These two methodologies have been compared in (Smirnova et al., 2010) considering a honeycomb absorber structure both at the single channel (discrete approach) and at the cup level (continuum 3D representation). Similarly, Fend et al. (2013) applied both the discrete and the continuum representations to assess the effect of geometric changes at the single channel and cup scale. In this case, the single channel model was exploited also to compute the volumetric heat transfer coefficient to be used in the continuum model.

Wu et al. (2011) developed a CFD macroscopic model of a porous absorber based on a ceramic foam adopting the continuum approach. The model considers the radiation transport in the media, as well as the energy balance for both the solid and the fluid phase. The heat transfer between the solid and the fluid phase is modeled introducing a local heat transfer coefficient based on the available correlations for porous medium, valid only for the fully developed flow region.

Kribus et al. (2014) parametrically analyzed a porous volumetric absorber by means of a simplified 1D model based on the continuum approach. The absorber was modeled as a homogeneous medium comprising two phases, namely the solid porous absorber and the fluid (air) flow. To compute the heat transfer between these two phases, an averaged convection coefficient per unit volume based on correlations was introduced, which does not consider the spatial variations that can be determined only with a detailed analysis at the pore-scale using the discrete approach. The low computational cost of the model allowed a wide parametric study, which included the porosity, the pore size, the thermal conductivity of the absorber material and the optical selectivity of the absorber surface.

Roldan et al. (2016) developed a 2D CFD model to assess the influence of the wind speed and incidence angle on the efficiency of a volumetric honeycomb receiver, as well as the effect of the return air speed and temperature. The two-dimensional computational domain (plane perpendicular to the receiver front face) allowed keeping a reasonable computational cost while considering four adjacent cups, with the honeycomb absorber approximated as a porous-medium, the air return channels between the cups and a portion of the external air in front of the receiver. However, this model cannot simulate the entire (3D) receiver and does not consider the detail of the pore-scale.

Capuano et al. (2017) numerically evaluated the thermal performance of a new absorber structure for volumetric honeycomb receivers at the single channel level using a 3D CFD model; hence, adopting a discrete approach. The model was validated against experimental data obtained from a lab-scale prototype, but it was not scaled up to simulate the entire receiver behavior.

Zhu and Xuan (2017) developed a pore-scale model (discrete approach) of a packed bed volumetric receiver where the Monte Carlo ray-tracing method is adopted to determine the radiation propagation inside the porous absorber.

Cagnoli et al. (2017) presented a coupled optical and CFD analysis of a single channel of a honeycomb volumetric receiver (discrete method). The heat flux distribution over the channel surfaces was determined by means of the optical analysis conducted with a ray-tracing software, while a detailed 3D CFD model was used to parametrically study the channel performance for different configurations and speeds of the air at the channel entrance (i.e., mass flow rate).

Du et al. (2018) proposed a new optimization method for porous volumetric receivers, which couples a metaheuristic optimization method based on the genetic algorithm and the heat transfer analysis. The latter was conducted by means of a CFD model based on the continuum representation of the absorber, simulated as a homogeneous porous medium consisting of two phases (solid structure and air flow) at different temperature. The genetic algorithm is then coupled with the CFD model to search for the best performing configurations.

Teng and Xuan (2018) proposed a new volumetric receiver concept, which exploits a cavity-like design to drastically reduce the radiative losses. A 2D CFD model was developed to simulate the thermal-hydraulic behavior of the cavity. In this model the absorber structure was treated as an isotropic and homogenous porous medium (continuum approach) where the absorber structure and the air flow locally have a different temperature and the convective heat transfer between the two phases is determined by means of Wu's correlation (Wu et al., 2011b).

A very recent work conducted by Stadler et al. (2019) aimed at developing a numerical model able to estimate the thermal performance of open volumetric receivers at the whole receiver scale. The proposed approach consists of a CFD model that solves the external air flow surrounding the receiver (about 6 million of cells) coupled with a 1D steady-state finite element model of the absorber structure.

In this paper, a novel multi-scale numerical approach is proposed, which combines the detailed discrete and the simplified continuum representations up to the whole receiver level. The aim of this methodology is to develop, in the

Modelica environment (Modelica Association, 2018), an accurate model of the whole receiver, keeping the computational cost as low as possible. The latter is a key requirement in order to exploit the receiver model also to simulate transient conditions.

The main novelty of the work presented in this paper is in scaling-up the numerical model up to whole receiver, whereas similar previous works combining discrete and continuum approach stopped at the cup scale (Fend et al., 2013; Smirnova et al., 2010). Moreover, in those previous studies the cup model was characterized, at least partially, on the base of experimental results, while in this work the thermal-hydraulic parameters of the cup model are entirely derived from the single channel model (micro-scale). In addition, the heat flux distribution has been determined here by means of an optical ray-tracing analysis, whereas in the above-mentioned studies by other authors an exponential law was assumed for the penetration of the concentrated solar radiation in the absorber structure, based on an empirically derived extinction coefficient.

If compared with the work of Stadler et al. (2019), the model presented here is more focused on the absorber porous structure (internal air flow), which is modeled by means of a multi-scale approach. On the other hand, the model of Stadler is able to evaluate the complex external air flow established in front of the receiver (not computed in our model), which is a relevant advantage since, for example, it can directly calculate the air return ratio distribution over the receiver surface taking into account its effect on the receiver performance. However, the model of Stadler is steady-state, while the receiver model developed here aims at simulating transient scenarios and it can be easily coupled with other models of the main plant components to simulate the dynamic behavior of the whole plant.

The dynamic behavior of the whole receiver has already been investigated by means of lumped-parameter models developed in the Modelica language in previous works (Ahlbrink et al., 2009; Hirsch et al., 2011; Yebra et al., 2005), which, however, adopted a simplified receiver model that does not take advantage of a detailed analysis at the single channel scale using the discrete approach.

The paper is organized as follows: the new multiscale approach is presented in Section 2; the geometry of the volumetric receiver, as well as the material adopted for the absorber structure, are defined in Section 3. The models developed for this study are introduced in Section 4, starting from the micro-scale (single channel) and going up to the macro-scale (whole receiver). At each scale, the input data obtained from the smaller scales, as well as the output data computed to characterize the models at larger scales, are highlighted. Finally, the results obtained applying the multiscale procedure to some test cases are presented and discussed in Section 5 and the main conclusions are summarized in Section 6.

2 Functional analysis of the receiver as a basis of the multiscale approach

From the operational point of view, we are interested only in a model of the whole receiver (macro scale), which, e.g., allows considering the proper driver of the 2D incident heat flux map. However, the dynamics at this scale is affected by many phenomena that one cannot afford to handle in detail at that scale, but only at the smaller scales. For instance the flow and temperature fields induced by the heat load on the channel surfaces can only be considered at the micro-scale level because of the computational cost that prevents including those details at the macro scale. Luckily, the modular nature of an open volumetric air receiver (see Figure 1) naturally allows a multi-scale approach to its modeling.

The methodology proposed in this work consists in scaling-up the receiver numerical model, from the micro-scale to the macro-scale with the aim of developing a tool capable to reproduce the dynamic behavior of the whole receiver. Starting from the (micro-scale) 3D numerical optical plus CFD model of the single channel, which allows characterizing the hydraulic (friction) and thermal (convective heat transfer coefficient) behavior of the channel, the receiver is studied at the cup level (meso-scale). The cup is modeled, in the Modelica environment, as a 1D porous medium with homogenized properties; thermal drivers are set according to the optical analysis. Specifically, on the front (irradiated) face of the cup a uniform heat flux is assumed, while the solar radiation absorbed inside the porous structure is reproduced by means of a volumetric heat source, function of the position along the air stream direction. Moving from the meso to the macro-scale level, a Modelica model is built to describe the entire receiver behavior. The receiver is modeled as a matrix of cups exploiting the meso-scale analysis, and including also the air return flow at the boundary of the porous structure. The cups differ only from the incident concentrated solar radiation point of view, since its distribution on the receiver surface is generally non-uniform. Figure 2 summarizes the multi-scale approach briefly described in this section.

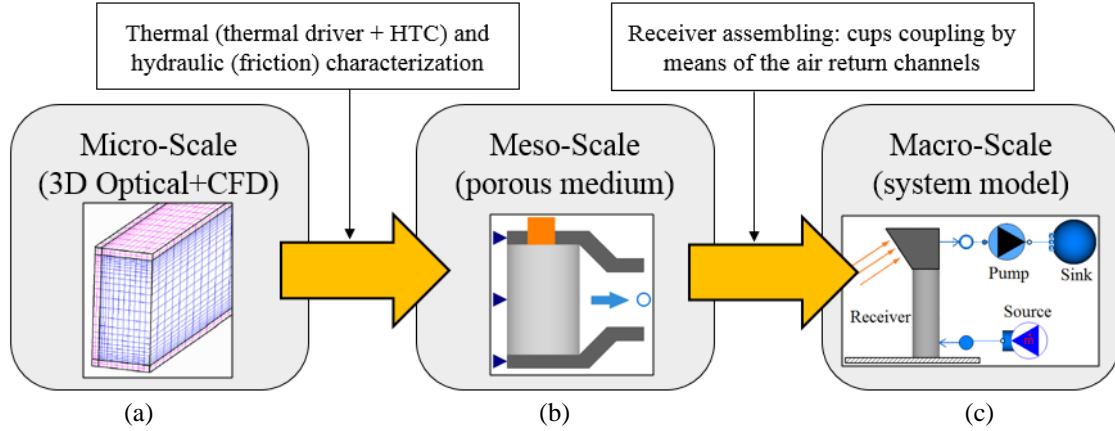


Figure 2 – Scaling up from the single channel (micro-scale) 3D Optical+CFD analysis (a) to the cup (meso-scale) 1D porous medium Modelica model (b) up to the whole receiver (macro-scale) Modelica model.

3 Definition of geometry and material

The receiver tested during the SolAir experimental campaign (Télez, 2003), consisting of 36 equal square-shaped cups having an edge length of about 130 mm (see Figure 1a), is considered as a reference design in this paper. However, the details of the receiver geometry are not publicly available at the best of the authors' knowledge (see also Cagnoli et al. (2017)); therefore, some assumptions have been introduced. In particular, the cup absorber structure is imposed to be made of a matrix of 52x52 prismatic channels, with a square cross section of side $L = 2$ mm and a wall thickness w equal to 0.25 mm (see Figure 1c), which correspond to values already adopted in the literature (Fend et al., 2013). With the assumed edge L and wall thickness w , the resulting porosity is 0.64, which is different from the porosity of the reference receiver (SolAir 200) that was 0.495. The channel depth d is set to 100 mm, as imposed in Cagnoli et al. (2017). This depth is not optimized for the receiver configuration investigated here, for which a shorter channel could be profitably adopted. However, this depth was chosen in Cagnoli et al. (2017) to ensure that a negligible amount of photons is able to leave the channel from the back aperture for any channel configuration considered in that study, which also included channels with increased aperture size (i.e., deeper rays penetration). The absorber depth will be reduced to 50 mm at the macro-scale level (section 4.3), once the meso-scale (cup) model will be successfully validated against the detailed micro-scale (single channel) model, as shown in section 4.2.3. The receiver tilt angle is 53° , which is the reference inclination for the given heliostat field, as explained in Cagnoli et al. (2017). Adjacent cups are separated by an air gap of assumed thickness equal to 6 mm, as shown in Figure 1a.

The absorber material is assumed to be Siliconized Silicon Carbide (SiSiC), which had been already adopted in the SolAir 200 project (Télez, 2003). Table 1 summarizes the material properties adopted in this study. The irradiated front face of the receiver is assumed to be covered with a selective coating in order to increase the solar absorptivity and reduce the thermal emissivity. This means that the absorptivity and the emissivity of the front face is different from that of the internal (not coated) wall surfaces of the absorber porous structure, according to Table 1.

Currently, the stability of selective coatings at high temperature is still an open issue and non-selective paints are typically used. The Pyromark (non-selective) paint represents the current state of the art for the coating of this kind of receivers, which ensures a high absorptivity (≈ 0.95), but not a low emissivity that is about 0.9 at 1000 °C (Ho et al., 2013). However, the stability of the selective coatings at high temperatures is a research topic widely addressed in the recent years (Al-Rjoub et al., 2018; Pang, 2017); therefore, this limit will be likely overcome in the next future. For this reason, selective coating properties according to Cagnoli et al. (2017) have been considered here; see Table 1.

Regarding the thermal emissivity of the internal (not coated) walls, it has been set equal to the optical absorptivity of the material, according to the Kirchhoff's law, see Table 1 again. Sani et al. (2012) observed that the SiC emissivity varies between 0.6 and 0.8 in the range 1100 – 1400 K; however, the material behavior at lower temperatures is not known. A sensitivity study has been carried out using the final receiver model, which shows that the thermal receiver efficiency only increases of less than 1% reducing the emissivity from 0.8 to 0.6. Therefore, the simplification based on the Kirchhoff's law has been adopted in this work.

Table 1 – Material properties adopted in this study

Reflectivity	Frontal face (selective coating)	0.1
	Internal walls	0.2 (Sani et al., 2012)
Emissivity	Frontal face (selective coating)	0.4
	Internal walls	0.8
Thermal conductivity (W/m K) @ 1000 °C		40 (FCT-Keramik, 2015)

4 Model description

4.1 Micro-scale model

The micro-scale analysis focuses on a single prismatic channel. The aim of this analysis is to characterize the single channel from both the hydraulic (pressure drop along the channel) and thermal (local convective Heat Transfer Coefficient HTC) point of view in steady-state conditions.

A detailed description of the methodology and analysis performed at the single channel level has been already presented in Cagnoli et al. (2017) for a number of different channel geometrical configurations and inlet air speeds, therefore it will be only briefly summarized here. First, an optical analysis has been conducted using Tonatiuh, a Monte Carlo ray-tracer (Blanco et al., 2005), in order to determine the absorbed heat flux distribution on the irradiated channel surfaces. The latter is then exploited as a thermal driver in the steady-state 3D CFD model that solves a conjugate heat transfer problem including the convection with the internal flow, the conduction in the solid, the radiative heat transfer inside the porous absorber and the convective and radiative heat losses. The details about the micro-scale 3D CFD model, like the boundary conditions, the mesh adopted and the parametric space investigated are available in Cagnoli et al. (2017).

Processing the results of the CFD analysis, the pressure drop across the channel and the local convective heat transfer coefficient for different cross sections along the air stream direction can be determined. The local value of the HTC has been determined according to Eq. 1

$$H_z = \frac{\dot{\phi}_f}{T_{wall} - T_{bulk}} \quad (1)$$

Figure 3 shows the resulting trend of the convective heat transfer coefficient along the channel depth, which has been calculated for 50 different cross sections along the channel. The HTC sharply decreases from the channel entrance to a minimum value and then it slowly increases reaching an asymptotic value.

At very low air inlet speeds (0.25 m/s), the HTC increases after the minimum, reaching a maximum value and then decreasing again to the plateau. The peak at the channel entrance is expected to be significantly higher than in the fully developed region because of the thinner boundary thermal layer that leads to a bigger wall temperature gradient. The HTC decreases sharply from the inlet section due to the progressive thickening of the thermal boundary layer in the entry region. In the fully developed region, the HTC first slowly increases because the convective heat flux decreases slower than the term $(T_{wall} - T_{bulk})$; see Eq. 1. Finally, the HTC reaches a plateau, since no more variations occur in the heat flux transferred to the air flow and in the temperature difference between the inner walls and the air stream. Comparing Figure 4a-b, it can be noted that increasing the inlet speed, the slope of the temperature difference decreases as a consequence of the deeper air penetration in the channel. At 0.25 m/s the slope of the temperature difference approaches the one of the convective heat flux leading to the different trend observed in Figure 3.

The HTC trend observed in Figure 3 ($V_{in} > 0.25$ m/s) is qualitatively close to the distribution of the local volumetric heat transfer coefficient along the flow direction calculated by Wu et al. (2011), who considered a volumetric receiver made of a porous ceramic foam at constant wall temperature.

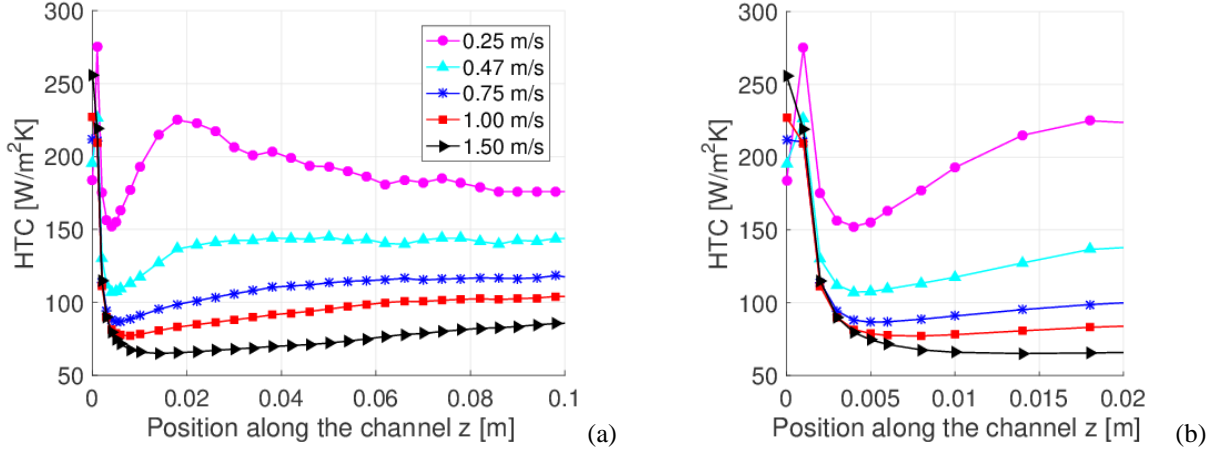


Figure 3 – (a) Convective heat transfer coefficient (HTC) along the channel computed processing the results of the CFD single channel model for different inlet air speeds given the absorbed power distribution. (b) Zoom on the first 2 cm of the channel length starting from the inlet section.

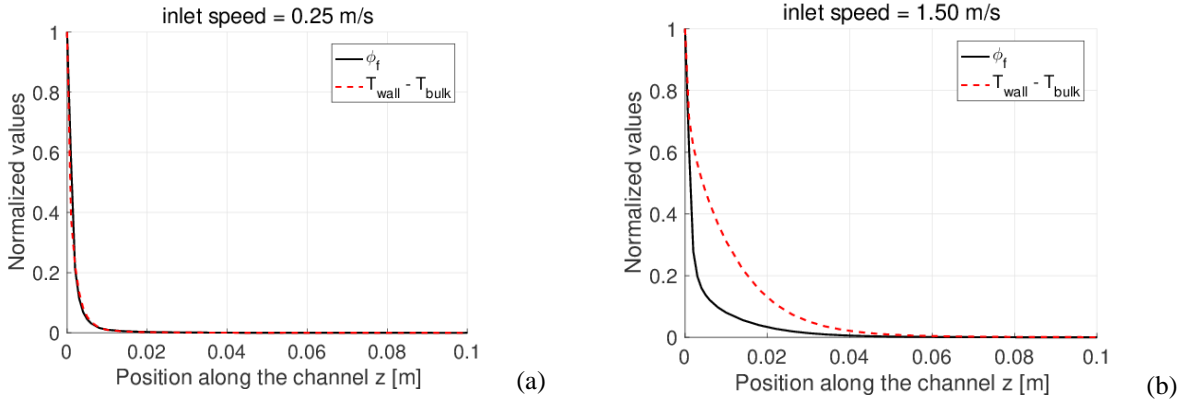


Figure 4 – Normalized convective heat flux transferred to the fluid (ϕ_f) and temperature difference ($T_{wall} - T_{bulk}$) computed using the CFD model at 0.25 (a) (c) and 1.50 (b) m/s

The asymptotic behavior of the HTC distribution is coherent with the theory; in fact, for a laminar fully developed flow the Nusselt number, and consequently the HTC, is expected to be constant and equal to 4.36 in the case of an imposed uniform heat flux (3.66 if a uniform wall temperature is imposed) (Incropera et al., 2012). Figure 3 shows that the value reached at the plateau by the HTC depends on the air inlet speed, i.e. on the air mass flow rate. This is mainly because at larger mass flow rate the air temperature decreases leading to a reduction of the thermal conductivity, which in turn determines a HTC reduction according to the definition of the Nusselt number Nu (Eq. 2).

$$Nu = H \times L/k \quad (2)$$

Figure 5a compares the HTC value at the plateau computed processing the CFD results with those obtained from the theory, on the basis of Eq. 1 where the air thermal conductivity is calculated at the average air temperature in the channel. The CFD-based heat transfer coefficient decreases with the inlet air speed quicker than those obtained from the theory; this is because the Nusselt number derived from the CFD analysis is not constant, but decreases with the air speed, since the wall temperature profile along the channel axis changes for different values of the air flow speed, see Figure 5b. Particularly, it tends to increase along the flow direction at low velocity magnitudes (as in the case of a uniform heat flux), while it is more or less constant along the channel axis for intermediate air speeds, reproducing the uniform wall temperature case. Finally, it slightly decreases at high air speeds as a consequence of the increased heat removal by the air flow when the mass flow rate rises.

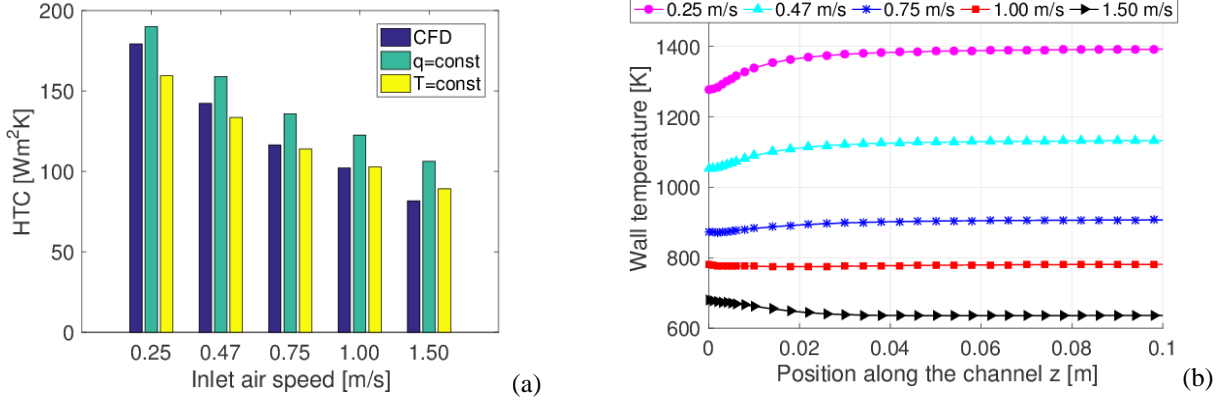


Figure 5 – (a) Comparison between the HTC computed using the CFD model and the HTC values obtained from the theory in the case of uniform heat flux ($q = \text{const}$) and uniform wall temperature ($T = \text{const}$) and (b) computed wall temperature profile along the channel axis at different air speeds.

4.2 Meso-scale model

At the meso-scale level, the cup absorber structure, typically consisting of thousands of channels (2704 in our case), is considered. Here the cup is modeled as a 1D (along the air stream direction) porous medium, characterized by the Darcy-Forchheimer friction law (Nield and Bejan, 1999), and by a non-equilibrium thermal model allowing heat transfer between solid and fluid phase. The computational gain in such an approach is the reduction of the dimensionality of the problem from a full 3D problem to a 1D problem along the stream direction. The other two dimensions are lumped into local constitutive relations for the friction factor (related to the normal gradient of the axial velocity profile at the channel walls) and for the heat transfer coefficient (related to the normal derivative of the temperature profile at the channel walls), which are derived from the micro-scale CFD model. The cup model has been implemented in the Modelica language.

The boundary conditions required at the cup inlet and outlet to solve the mass, momentum and energy balance are summarized in Figure 6a, and include pressure and temperature of the air inlet flow, the air mass flow rate sucked from the cup rear side by the blower and the thermal driver. The latter consists of a uniform heat flux applied on the cup front face plus a space-dependent volumetric heat source in the absorber body. The uniform distribution assumption is justified because of the relatively small size of the single cup that guarantees a negligible change of the heat flux over its front face, for any reasonable aiming strategy. In this study, both the volumetric heat source and the uniform heat flux on the front face are determined according to the optical analysis already exploited at the micro-scale level and presented in Cagnoli et al. (2017). Finally, the rear side of the solid phase is assumed to be adiabatic, while the front face can lose heat by convection and radiation.

At the inlet, the cup absorber structure sucks air directly from the ambient; hence, a fixed value of pressure, equal to the atmospheric value (≈ 1 bar) has been imposed. The air inlet enthalpy (h_{in}) is calculated assuming an adiabatic mixing between the fresh air and the recirculated share, as

$$h_{in} = ARR \times h_{return} + (1 - ARR) \times h_{amb} \quad (3)$$

The so-called Air Return Ratio (ARR) is defined as the share of the total air mass flow rate (\dot{m}) that is actually recirculated in the absorber structure (\dot{m}_{return}).

$$ARR = \frac{\dot{m}_{return}}{\dot{m}} = \frac{\dot{m}_{return}}{\dot{m}_{return} + \dot{m}_{amb}} \quad (4)$$

where, as shown in Figure 6b, part of the air coming from the apertures between adjacent cups is lost to the environment and has to be replaced with fresh air at ambient temperature (\dot{m}_{amb}).

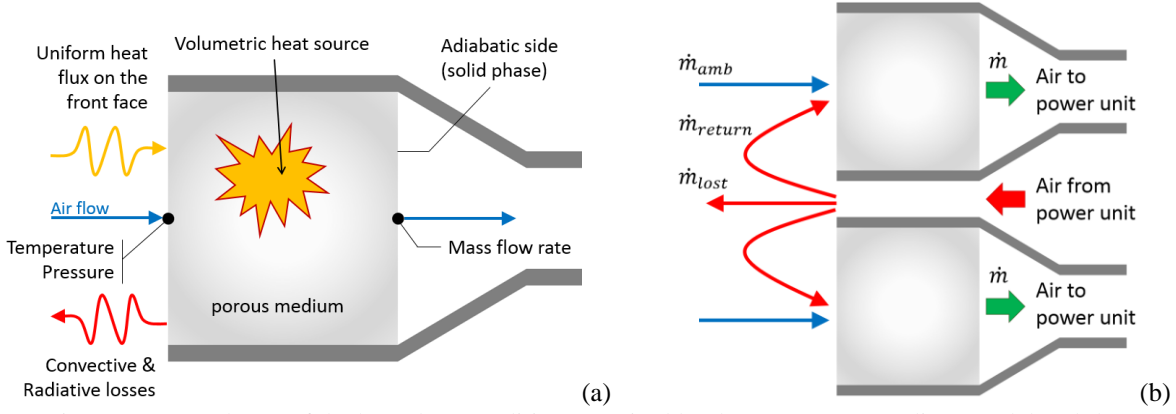


Figure 6 – (a) Scheme of the boundary conditions required by the cup porous medium model and (b) mass flows involved in the ARR definition

4.2.1 Hydraulic model

The hydraulic model solves the mass and the momentum balance equations. The former is given for the i -th control volume (CV) of the 1D spatial discretization by

$$V_{f,i} \frac{d\rho_i}{dt} = \dot{m}_{in,i} - \dot{m}_{out,i} \quad (5)$$

The air density (ρ) is computed by means of the ideal gas law. The accumulation term ($d\rho/dt$) has been neglected in this model since a very limited amount of air can be stored inside the porous structure due to the very low air density. Therefore, the simplified mass balance implemented in the meso-scale model can be written as

$$\dot{m} = \dot{m}_{in,i} = \dot{m}_{out,i} \quad (6)$$

The momentum balance is based on the Darcy-Forchheimer law, applied along the flow direction (z axis), as

$$\left(\frac{\partial p}{\partial z} \right)_i = -\frac{\mu_i}{K} \phi u_i - \frac{J}{\sqrt{K}} \phi^2 (\rho u^2)_i \quad (7)$$

The air viscosity (μ) is computed as a function of the temperature and the air speed (u) is the average value over the fluid volume. The medium porosity ϕ is a key geometric parameter that characterizes the absorber structure, defined as the fraction of the volume of voids over the total volume (see Eq. 8); K and J are the permeability of the porous medium and the inertial coefficient respectively. Eq. 7 is written in a steady-state form for the sake of simplicity, since we are not really interested in an accurate estimation of the pressure during a transient. Moreover, the time rate of change of the linear momentum of the fluid is likely to be negligible if compared with the linear (friction) and quadratic (inertial) terms in Eq. 7, because of the limited reasonable changes of the air speed during a transient.

The porosity can be immediately determined according to

$$\phi = \frac{L^2 \times d}{(L + 2w)^2 \times d} = 0.64 \quad (8)$$

In order to determine the value of K and of the inertial coefficient J , Eq. 7 is re-written in dimensionless terms (Eq. 9), following the methodology in (Zanino and Savoldi Richard, 2006).

$$f_k = \frac{1}{Re_K} + J \quad (9)$$

f_k and Re_k are the friction factor and the Reynolds Number, respectively, defined using the square root of K as the characteristic length, i.e.

$$f_k = \frac{\Delta p}{d} \frac{\rho A_f^2 \sqrt{K}}{\varphi^2 \dot{m}^2} \quad (10)$$

$$Re_k = \frac{\dot{m} \varphi \sqrt{K}}{\mu A_f} \quad (11)$$

A set of hydraulic simulations have been run then using the single channel CFD model. Each simulation is characterized by a pair air mass flow rate (i.e. inlet air speed) and air temperature, the latter only affecting the air properties in a pure hydraulic simulation. Table 2 summarizes the values considered.

Table 2– Values of air temperature and inlet air speed used in the pure hydraulic simulations

Air temperature [K]	Air inlet speed [m/s]
300	0.25
800	0.75
1300	1.50

From each simulation, the pressure drop across the channel has been extracted. Then, Eqs. 9, 10 and 11 have been solved iteratively to find the best fit ($R^2 \approx 1$) of K and J that satisfied both the friction factor and Reynolds number definitions (Eqs. 10 and 11) and the dimensionless Darcy-Forchheimer law given by Eq. 9. Figure 7 shows the result of this procedure, which provides a permeability K equal to about $9.20 \times 10^{-8} \text{ m}^2$ and an inertial coefficient J around 0.003.

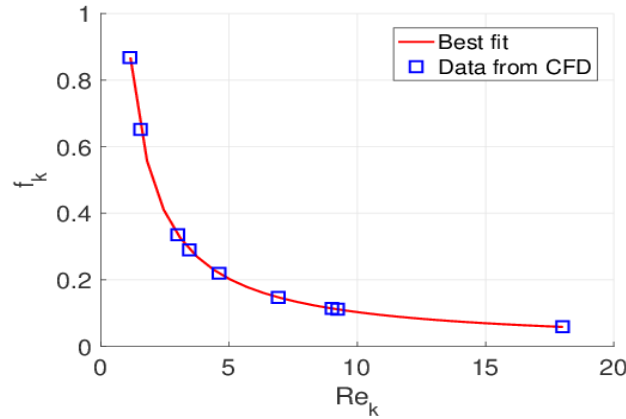


Figure 7 – Best fit of the permeability K and the inertial coefficient J . Each point corresponds to a pure hydraulic simulation performed with the single channel CFD model.

While the Darcy-Forchheimer law provides the pressure drop across the porous medium, the possible presence of an orifice at the very rear of the cup is accounted for at the whole receiver level (macro scale), to regulate the mass flow rate in the receiver cups according to the (non-uniform) heat flux distribution. At the meso scale, the orifice could be included in the cup model as an imposed minor loss located at the porous medium outlet.

4.2.2 Non-equilibrium thermal model

The 1D non-equilibrium porous medium model solves the energy balance equations in both the solid and fluid phases. Starting from the solid phase, the energy balance is given by

$$V_i \Phi_{vol,i} = \rho_s c_s V_s \frac{dT_s}{dt} + \phi_{f,i} + \Delta \phi_{cond,i} + \phi_{AR,i} + \phi_{loss,i} \quad (12)$$

The dynamic term of the equation describes the solid phase temperature evolution over time (dT_s/dt) considering the solid material properties and the volume occupied by the solid region. Figure 8 shows a sketch of the porous cup model, including the main heat fluxes computed by the model.

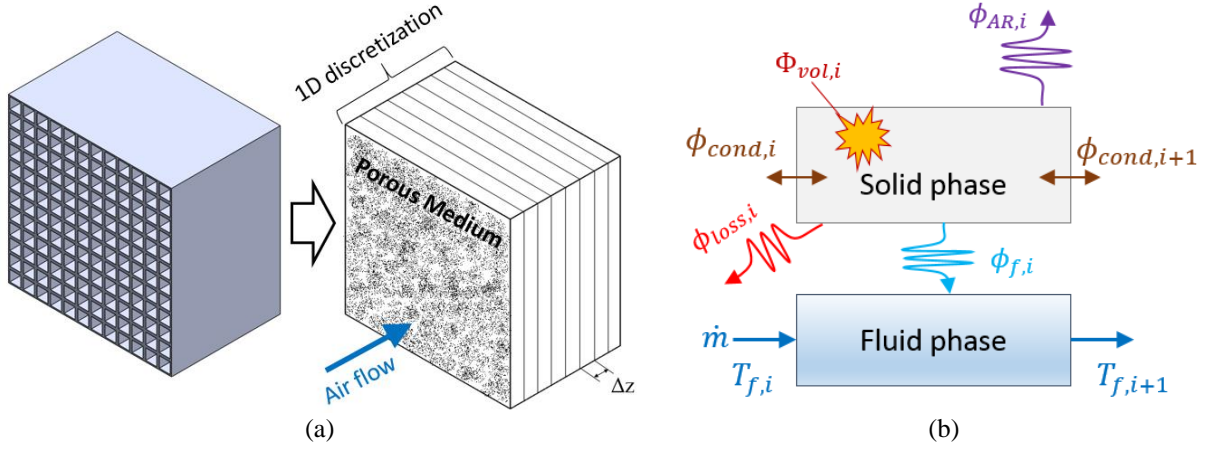


Figure 8 – (a) From the honeycomb absorber to the homogenous porous medium approximation, with the 1D space discretization along the flow direction highlighted and (b) schematic representations of the heat fluxes computed at the i -th control volume of the 1D discretization.

The convective heat ϕ_f transferred to the air stream is given by

$$\phi_{f,i} = H_{z,i} A_v V_i (T_{s,i} - T_{f,i}) \quad (13)$$

The local heat transfer coefficient (H_z) is obtained processing the CFD results at the single channel level (Figure 3) as a function of the position along the z axis and of the air mass flow rate. The heat transfer surface per unit volume (A_v) is a geometric parameter defined as the ratio between the effective heat transfer surface in the porous medium and the volume of the medium itself. Knowing the channel geometry, A_v can be immediately determined as

$$A_v = \frac{4L \times d}{(L + w)^2 \times d} = 1280 \text{ m}^{-1} \quad (14)$$

The net conductive heat $\Delta\phi_{cond,i}$ is approximated using the central difference scheme as

$$\Delta\phi_{cond,i} = -k_s \times A_s \frac{T_{s,i-1} - 2T_{s,i} + T_{s,i+1}}{\Delta z} \quad (15)$$

Two boundary conditions are imposed as follows:

$$z = 0 \rightarrow \ddot{\phi}_{cond,1} = \ddot{\phi}_{sol,front} - \ddot{\phi}_{rad,front} - \ddot{\phi}_{conv,front} \quad (16)$$

$$z = d \rightarrow \ddot{\phi}_{cond,end} = 0 \quad (17)$$

In Eq. 16 the convective and radiative heat losses from the solid front face ($z = 0$) have been taken into account, as well as the directly absorbed solar radiation. In Eq. 17, an adiabatic condition has been imposed at the outlet section ($z = d$). The heat flux absorbed on the front face ($\ddot{\phi}_{sol,front}$), assumed to be uniform, comes from the optical analysis, while the radiative ($\ddot{\phi}_{rad,front}$) and convective ($\ddot{\phi}_{conv,front}$) heat losses from the front face are given by

$$\phi_{rad,front} = \sigma \varepsilon_c A_s (T_{s,1}^4 - T_{amb}^4) \quad (18)$$

$$\phi_{conv,front} = A_s H_{ext} (T_{s,1} - T_{amb}) \quad (19)$$

Note that the emissivity ε_c is that of the selective coating applied on the front face (see Table 1). H_{ext} is the convective heat transfer coefficient between the front face and the external ambient, which has to be imposed in the model, while $T_{s,1}$ is the solid temperature at the first CV. The radiative heat losses from the inner surfaces of the cup porous structure to the environment are given by

$$\phi_{loss,i} = F_{i,ext} \times A_v V_i \times \sigma \varepsilon_s (T_{s,i}^4 - T_{amb}^4) \quad (20)$$

where $F_{i,ext}$ is the view factor between the inner walls and the external ambient at the control volume i and the product $A_v V_i$ provides the actual heat transfer surface in the volume V_i . In this case the thermal emissivity ε_s is that of the solid material (no selective coatings). Finally, the heat transferred to the air return flow, ϕ_{AR} in Eq. 12, is computed only if the cup porous medium model presented here is coupled with the model of the air return channel, as explained below in Section 4.3 (macro-scale) where ϕ_{AR} is defined (Eq. 25).

Regarding the fluid phase of the porous medium, the transient energy balance equation, assuming negligible changes in the pressure head, air speed and potential energy between the outlet and inlet sections of the control volumes, can be written as

$$A_f \Delta z \frac{d(\rho h - p)_i}{dt} = (\dot{m}_{in} h_{in} - \dot{m}_{out} h_{out})_i + \phi_{f,i} \quad (21)$$

The net enthalpy flow across the control volume is calculated considering the inlet/outlet values of mass flow rate (\dot{m}) and specific enthalpy (h). Starting from Eq. 21 some further simplifications can be done:

- First, the dynamic term $d(\rho h - p)_i/dt$ can be neglected, since the heat capacity of the fluid phase in the cup porous structure is significantly lower ($\approx 10^3$ times) than that of the solid phase.
- Then, according to the continuity equation (Eq. 6) the mass flow rate across the inlet section of the i -th control volume is the same of the mass flow rate across the outlet section ($\dot{m}_{in} = \dot{m}_{out} = \dot{m}$).

According to these simplifications, Eq. 21 can be rewritten as

$$0 = \dot{m}(h_{in} - h_{out})_i + \phi_{f,i} \quad (22)$$

Note that, in the end, the only accumulation term computed by the cup model is the time derivative of the solid temperature in Eq. 12. As discussed above, this simplification is justified because of the low density and heat capacity of the air in the cup, which results in a negligible mass and energy accumulation in the fluid phase contained in the system. Therefore, the model is expected to well reproduce also the dynamic behavior of the absorber medium.

4.2.3 Benchmark of the cup model

The 1D cup model alone (not coupled with the return air flow) should reproduce the results obtained using the micro-scale CFD analysis in steady-state conditions. To check that, a set of simulations have been run, changing the inlet air speed (i.e. the mass flow rate) and the absorbed heat flux magnitude. In this analysis, the ambient temperature has been set equal to 300 K, which corresponds to the air inlet temperature since the air return flow is not considered here (ARR = 0) because it is not included in the single channel (micro-scale) model. Regarding the heat flux absorbed on the front face, the nominal value adopted in this analysis is 400 kW/m². The discretization along the flow direction adopted in this study consists of about 30 control volumes, which are sufficient to make the results independent by the number of nodes.

Figure 9a compares the temperature of the air outflow and of the solid front face computed with the single channel and with the cup model for different air inlet speeds, while in Figure 9b the absorbed heat flux has been varied by $\pm 30\%$ at given air inlet speed (0.75 m/s).

According to Figure 9a, the 1D cup porous medium model is able to reproduce the results obtained with the 3D single channel model; the deviation is always lower than 10% ($\sim 4\%$ on average). This deviation can be considered acceptable in view of the much (more than two orders of magnitude) lower computational cost of the continuum cup model. The qualitative achievement of the volumetric effect, for all but the highest air inlet speeds, is confirmed by both models, see Cagnoli et al. (2017) for a discussion of this feature. Figure 9b proves that the cup porous medium model is adequately robust, since it evaluates the air outlet temperature and the solid front face temperature, in the range of heat fluxes tested, with approximately the same accuracy demonstrated in the nominal case.

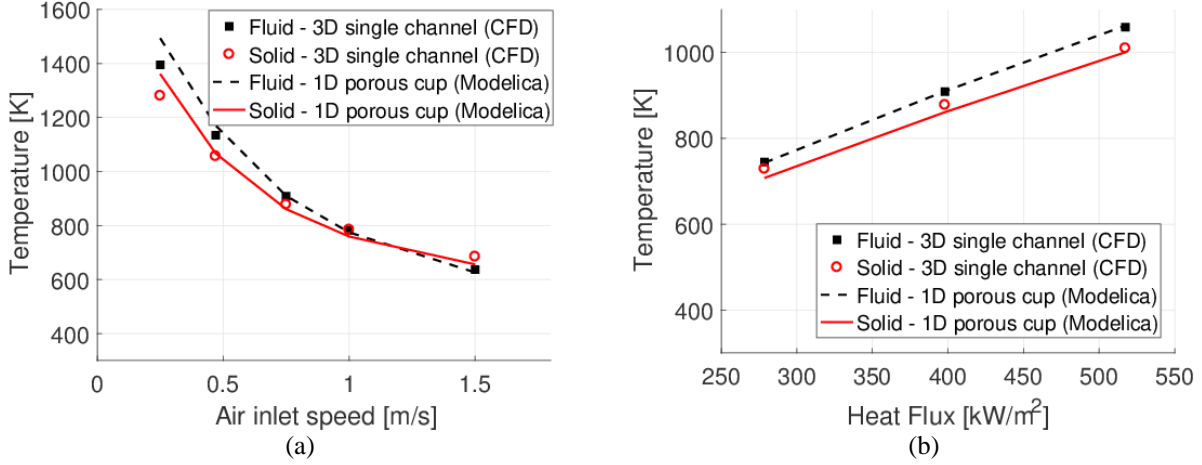


Figure 9 – Air outflow and solid front face temperature computed with the single channel CFD model (symbols) and with the 1D porous medium cup model (lines): effect of mass flow rate at given absorbed heat flux = 400 kW/m² (a) and of absorbed heat flux at given air inlet speed = 0.75 m/s (b). The y-axis minimum value corresponds to the air inlet temperature (300 K) to show the temperature increase along the absorber.

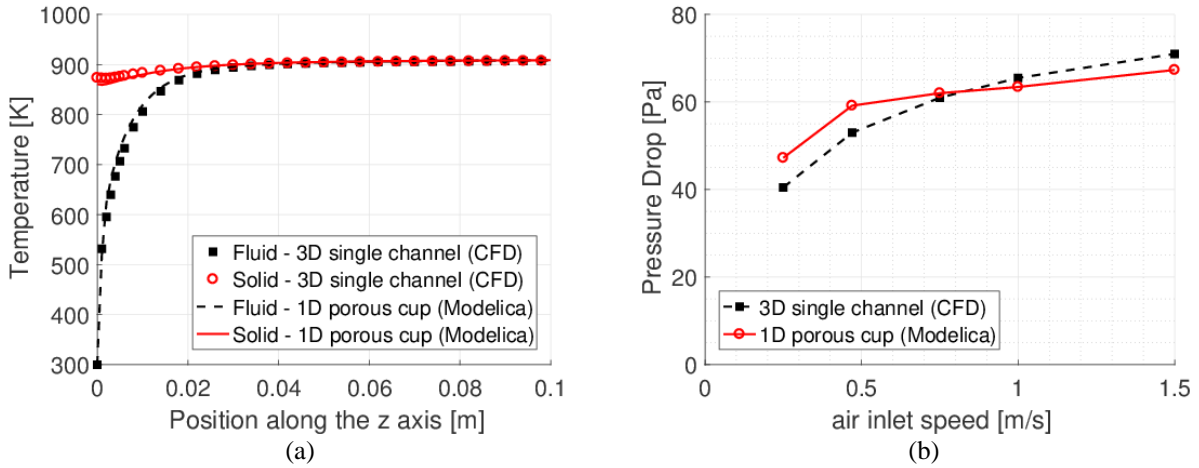


Figure 10 – (a) Fluid and solid temperature distribution along the absorber structure calculated with the 1D porous cup model (lines) and with the 3D CFD single channel model (symbols) and (b) comparison between the pressure drop evaluated using the cup and the single channel model for different mass flow rates.

The capability of the cup model to reproduce the temperature distribution of both the solid and fluid phases along the flow direction has been evaluated, see Figure 10a, in the case of an inlet air speed equal to 0.75 m/s and considering the nominal absorbed heat flux. Figure 10b, instead, displays the comparison between the two models in terms of pressure drop across the absorber, assuming no pressure loss at the rear orifice (not considered in the single channel model), for different air inlet speeds.

At low air speeds, the relative deviation between the pressure drop computed with the cup model and with the single channel model is not completely negligible; see Figure 10b. Specifically, it is $\approx 17\%$ at 0.25 m/s and $\approx 12\%$ at 0.47 m/s, while it decreases to 5% or lower at higher speeds. The reason for this relatively high deviation at low mass flow rates is in the difference between the fluid temperatures obtained using the two models that is higher at low air inlet speeds (see Figure 9a). This difference in the computed temperature determines a much more evident deviation in the estimated pressure drop, since the Darcy term of the momentum balance (i.e. the first term on the right-hand side of Eq. 7) increases almost quadratically with the temperature due to the dependence of the dynamic viscosity and of the air speed from the temperature. Figure 10a suggests that, for the given absorber configuration, a depth of about 50 mm is enough to heat the air flow up to the outlet value. For this reason the absorber depth has been shortened in the macro-scale model (section 4.3.2 and 5).

4.3 Macro-scale model

The aim of the macro-scale analysis is to describe the whole receiver thermal behavior in order to predict its performance in both steady-state and transient operation. The main peculiarity of the macro-scale level is the possibility to take into account the effect of the non-uniform (concentrated solar) heat flux distribution on the receiver, as well as the air return flow, which cannot be considered at the lower scales.

The macro-scale receiver model can be modularly generated in the Modelica environment, since the open volumetric receiver basically consists of a matrix of equal cups, and the generic cup model is developed at the meso-scale, see Section 4.2.

The thermal coupling between neighboring cups is accounted for modeling the air gap between adjacent cups, where the air stream coming from the power unit flows and removes the heat from the absorber modules. At the same time, the effect of the recirculated air on the receiver performance is included in the model as described below.

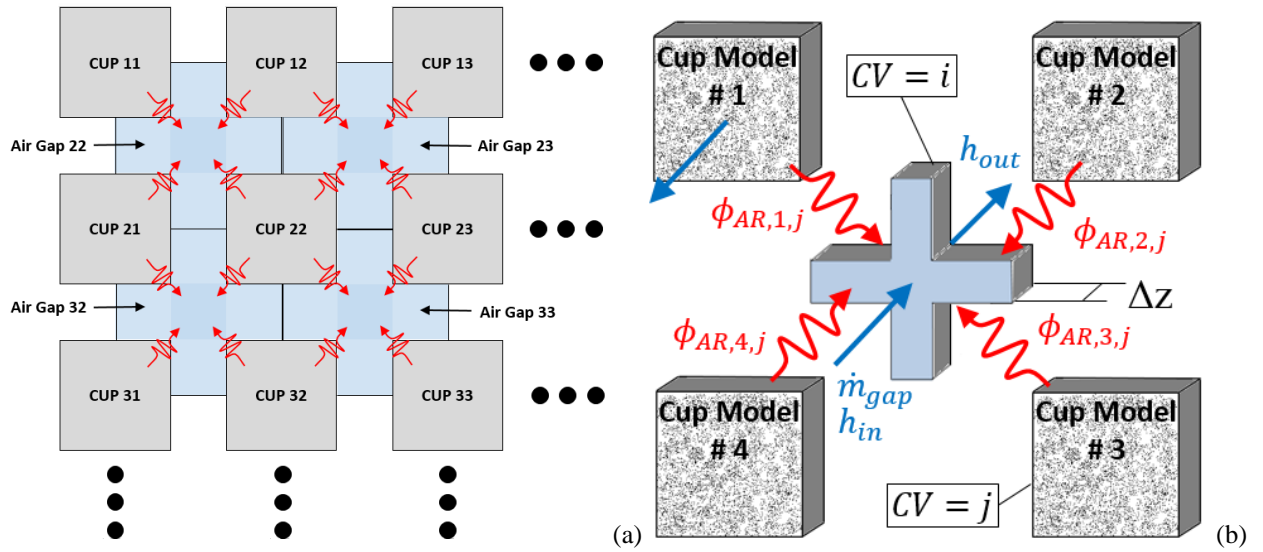


Figure 11 – (a) Schematic of the macro-scale model of the top left corner of the receiver, with the air gap discretized in a series of cross-shaped channels. The red arrows represent the heat transfer between the cups and the neighboring air return channels. (b) Scheme of the air gap model with the detail of the control volume i where the heat fluxes transferred from the surrounding cup models (j -th control volume) are highlighted together with the return air flow (mass flow rate \dot{m}_{gap} and specific enthalpy h) passing through the CV. The air flow in the cups has reversed direction as indicated in the cup #1.

The boundary conditions and thermal drivers required by the receiver model are summarized in Figure 12:

- Total mass flow rate extracted from the receiver rear side, which is distributed among the cups according to the pressure drop calculated in each absorber module, on top of which orifices can be introduced in the model.
- Total mass flow rate coming from the power unit and corresponding temperature. This mass flow rate is then divided among the air return channels according to the pressure drop calculated in each of them. The ARR must be provided as a parameter for each cup in the receiver.
- Ambient air temperature and pressure.
- Incident heat flux distribution, which is applied as a different (uniform) heat flux cup by cup.
- Volumetric heat source distribution, which is assumed not to change qualitatively with the incident heat flux, but it is simply scaled on the base of the heat absorbed on the front face.

In addition, the convective heat transfer coefficient between the receiver front face and the ambient air must be provided to calculate the convective heat losses, while the radiative losses are computed according to the absorber emissivity (see Section 4.2.2). The model considers only the heat flux incident on the cup front face, which is partially absorbed directly on the front face and partially absorbed on the internal walls of the porous medium (modeled with a volumetric heat source); however, a share of the solar radiation penetrates in the gap between the absorber modules.

This share of the incoming solar power (less than 10% for the receiver analyzed here) is absorbed on the lateral walls of the cup structure. However, it is included in the model increasing the heat flux incident on the cups by a factor equal to the ratio between the total receiver front area and the area of the receiver front face occupied by only the cups.

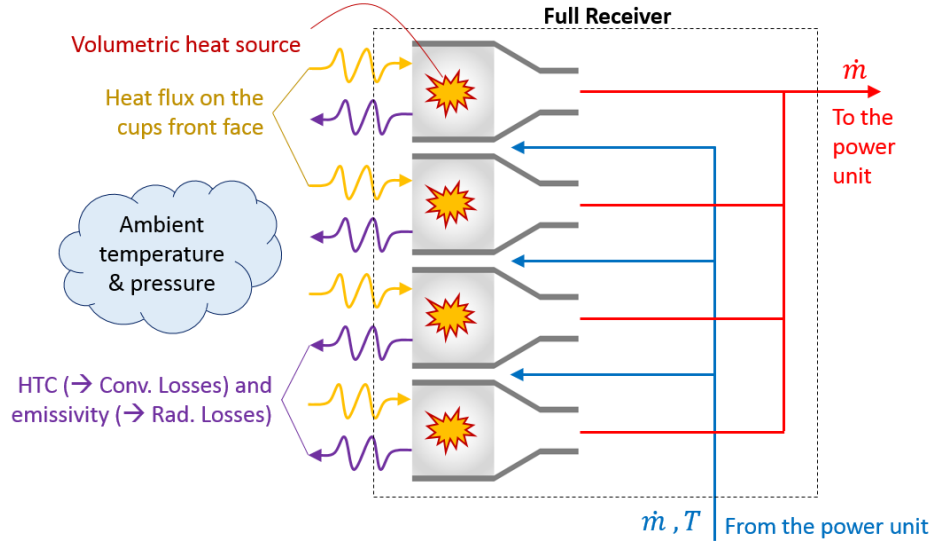


Figure 12 – Schematic of the full receiver model: boundary conditions and thermal drivers applied. The solar power that penetrates in the gaps is considered increasing the solar radiation incident on the cups that determines the heat absorbed on the front face and inside the porous medium (volumetric heat source).

4.3.1 Air gap model

The air gap has been modeled in 1D as a cross-shaped channel that thermally connects four different cups (two at the boundaries and one in the corners), see Figure 11. The air gap model solves the 1D mass, momentum and energy balance equations for the air stream that flows in the gap, considering the convective heat transfer with the adjacent cups. The assumption of negligible mass, momentum and energy transfer between contiguous air return channels is introduced with the aim of saving computational time.

Figure 11b provides a scheme of the air gap model, with the main fluxes considered. It has to be noted that the recirculated air in the gap flows in the opposite direction with respect to the air stream in the absorber (the first CV corresponds to the last CV of the cup). To couple the air gap model easily with the cup model, the same number of control volumes has been imposed (N_{cv}); therefore, the j -th control volume of the cup will be thermally coupled with the i -th control volume of the air return channel, where the relation between i and j is: $i = N_{cv} - j + 1$.

The mass balance in the air gap is the same already implemented in the cup model (Eq. 6). The momentum balance is solved for the air return channel as a whole with averaged fluid properties, and is given by Eq. 23.

$$\Delta p = f \frac{d}{D_{eq}} \frac{\dot{m}_{AR}^2}{2\rho A_{AR}^2} \quad (23)$$

The friction factor has been determined under the assumption of smooth pipe, which is here justified because this model does not aim at estimating with a high accuracy the pressure drop in the gap, but rather a realistic distribution of the mass flow rate among the air return channels. In order to solve Eq. 24, the ambient pressure is imposed as a boundary condition at the outlet section of the air return channel (i.e. the receiver front face).

The energy balance equation for the recirculated air stream has been formulated as in Eq. (24)

$$\sum_{x=1}^n \phi_{AR,x,j} = \dot{m}_{AR}(h_{in} - h_{out})_i \quad (24)$$

where $\phi_{AR,x,j}$ is the heat transferred by convection between the control volume j of the cup x , and the corresponding control volume i of the air gap model; see also Figure 11b. The heat transferred to the return air flow ($\phi_{AR,x,j}$) is

computed according to Eq. 25, where the surface temperature of the cup should be considered to calculate the convective heat transfer.

$$\phi_{AR,x,j} = H_{AR,i} A_{L,j} (T_{s,j} - T_{fm,i}) \quad (25)$$

However, due to the 1D nature of the cup model, $T_{s,j}$ is the average temperature along the transverse direction of the solid phase in the control volume. H_{AR} is the convective heat transfer coefficient between the lateral wall of the cup structure and the air return flow, which is determined for each CV as a function of the Nusselt number Nu (see Eq. 2), assuming that the flow is completely developed. In this case, the characteristic length (L in Eq. 1) corresponds to the hydraulic diameter D_{eq} , while Nu is calculated according to the Gnielinski correlation (Incropera et al., 2012), being the Reynolds number larger than 3000 at the inlet section of the air return channel.

4.3.2 Comparison with the SolAir 200 experiment

Three configurations have been tested during the SolAir project (Téllez, 2003); the first configuration is considered here for the comparison with the results obtained from the macro-scale full receiver model since data from the steady-state tests are available and the receiver consisted of identical cups. Among the 40 steady-state tests available for the first configuration, 11 tests have been selected, which cover the whole range of mass flow rate and incident solar power measured during the experiments.

In Table 3, the air outlet temperature and the corresponding efficiency will be used for the comparison with the outcomes of the receiver macro-scale model. For this purpose, we introduce the receiver performance defined as

$$\eta_{rec_solair} = \frac{\dot{m}(h_{out} - h_{amb})}{\phi_{in}} \quad (26)$$

Note that this definition leads to higher efficiency with respect to that calculated by other authors, for example (Stadler et al., 2019), that uses the return air enthalpy instead of the ambient one to define the efficiency.

The comparison presented in this section cannot be considered a full and detailed validation of the model because of the unavailability of some information about the absorber structure and the test conditions, see below.

- In the SolAir project the porosity was 0.495, however, the details of the cup structure (size of the channel cross section and thickness of the wall) leading to that porosity are not publicly available, at the best of the authors' knowledge. Therefore, we imposed the porosity of the SolAir absorber assuming the same channel aperture considered in Section 3 (2 mm), but a thicker wall.
- The actual depth of the absorber is not known, 50 mm is assumed here.
- The solar rays penetration in the porous medium depends on the medium porosity, the specific heliostat field and the inclination of the receiver, which are not the same in the experiment and in the model. Therefore, some differences in the distribution of the absorbed solar radiation inside the porous medium are expected.
- The mass flow rate distribution measured in the SolAir project is provided only in the case of cold air, but it will be slightly different under on-sun conditions because of the different air temperatures reached in the cups that affect the air properties. In this comparison, the cold air mass flow rate distribution is imposed in the model.
- The incident solar power was measured; however, we are interested in the absorbed power (net of the reflected photons); hence, the effective absorptivity of the receiver has to be assumed as discussed below.
- The distribution of the incident heat flux on the receiver surface, which depends on the aiming strategy, is not known; thus, a Gaussian distribution with standard deviation equal to 0.4 is arbitrarily assumed. The peak flux of the Gaussian distribution is set in such a way that the integral value of the heat flux distribution corresponds to the absorbed power.
- The ambient temperature and the inlet temperature of the return air are not explicitly provided; they have been derived from other available data, as explained below.

Table 3 – Data collected during the SolAir 200 experimental campaign for the configuration 1 of the receiver in quasi steady-state conditions (Téllez, 2003)

Test	Mass flow rate [kg/s]	Incident solar power [kW]	Power gained [kW]	Outlet temperature [K]	Efficiency [-]
1	0.378	254	224	874	0.882
2	0.356	258	212	876	0.822
3	0.383	313	248	925	0.790
4	0.374	309	260	971	0.841
5	0.377	334	273	994	0.817
6	0.364	345	279	1031	0.807
7	0.359	355	275	1029	0.773
8	0.345	389	282	1075	0.726
9	0.349	369	284	1073	0.771
10	0.298	227	185	902	0.814
11	0.320	276	225	975	0.813

The missing input to run the receiver model, which is not available in Table 3, includes the absorbed power, the ambient temperature and the inlet temperature of the air return flow. The former can be estimated introducing a reasonable absorptivity that multiply the measured incident solar power. For this purpose, it is assumed that the absorptivity is equal to the nominal value of the Pyromark paint ($\approx 95\%$ (Ho et al., 2013)) for the receiver front frame, while the radiation entering in the channels is assumed to be completely absorbed. The ambient temperature can be easily determined from the power gained data, which corresponds to the air enthalpy increase from the external ambient to the receiver outlet in Téllez (2003).

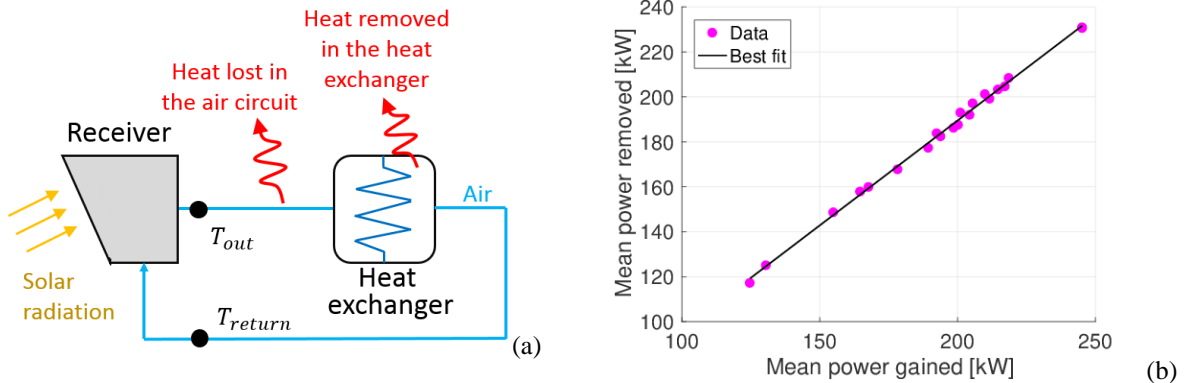


Figure 13 – (a) Sketch of the air circuit with the air/water heat exchanger and the main thermal power and temperature involved in the energy balance. (b) Power removed from the recirculated air mass flow rate downstream the receiver (SolAir 200 project) as a function of the measured (average) power gained and the corresponding linear best fit.

In order to estimate the temperature of the return air flow entering the receiver, an additional set of data has been considered, which provides the heat removed by the air/water heat exchanger downstream the receiver, as well as the heat losses that occurred in the air circuit (see Figure 13a). This information is not available for each of the steady-state test performed, but it is provided as a daily average together with the average value of the power gained; see Figure 13b. Both data from configuration 1 and 2 has been considered here, since the heat removed downstream the receiver does not depend on the receiver configuration. A linear fit of good quality ($R^2 \approx 0.997$) has been obtained from the considered data (see Figure 13b), which have been then exploited to estimate the heat removed from the recirculated air flow in the steady-state tests considered, given the power gained data in Table 3. Once the heat removed has been determined, the temperature of the recirculated air can be calculated from energy balance. The resulting absorbed solar power, ambient temperature and air return inlet temperature, are shown in Figure 14.

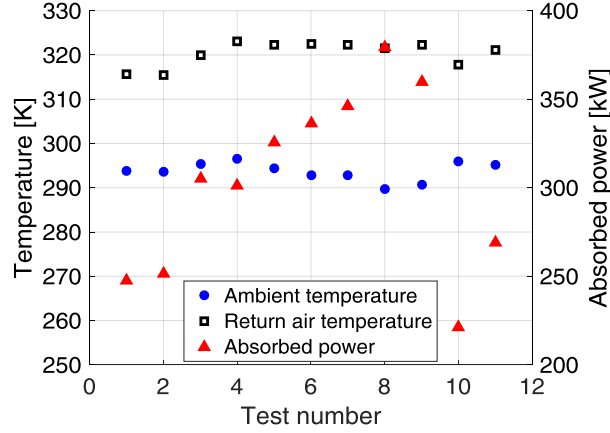


Figure 14 – Calculated inputs (absorbed heat plus ambient and return air inlet temperature) for the selected tests determined on the base of the available data.

In the simulations, the ARR is imposed to 0.4 (Téllez, 2003), the emissivity is 0.9, which is the value assumed by Téllez (2003) in the analysis of the SolAir measurements. The convective heat loss is calculated imposing a heat transfer coefficient with the external air equal to $10 \text{ W/m}^2\text{K}$, according to Ho and Iverson (2014), and considering the external air at ambient temperature. As proved by a sensitivity analysis (see Cagnoli et al. (2017)), the impact of the assumed value of the heat transfer coefficient is almost negligible because the heat losses are dominated by the radiative mechanism; for the same reason the considered air temperature may have a negligible influence on the receiver performance. The results of these runs are displayed in Figure 15, in terms of air outlet temperature (net of the ambient temperature) and efficiency, as a function of the ratio between the absorbed solar power and the mass flow rate, which corresponds to the specific energy available for the air flow. According to Téllez (2003), an error bar of ± 0.06 is added to the efficiency values determined from the experiments.

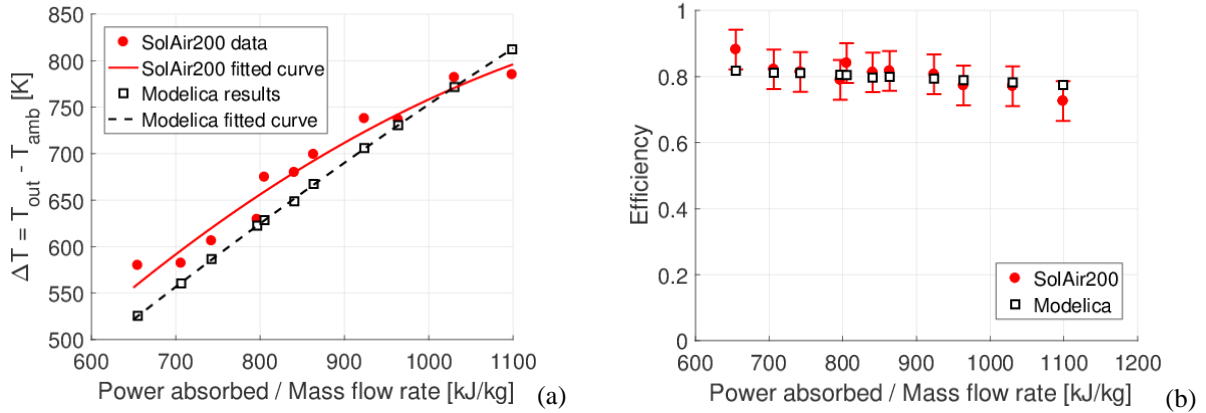


Figure 15 – Comparison between the results of the receiver macro-scale model and the SolAir 200 data in terms of (a) air temperature difference between the receiver outlet and the ambient and (b) efficiency as a function of the ratio between the absorbed power and the mass flow rate.

Figure 15 indicates that the results computed with the receiver macro-scale model match quite well those of the experiments, despite the differences discussed at the beginning of this section. In particular, Figure 15a shows that the computed air outlet temperature always fall within the error bar of the values measured during the SolAir experimental campaign.

5 Macro-scale results and discussion

In this section, the results from the full receiver model (macro-scale) are presented and discussed. The receiver considered here consists of a 6x6 matrix of cups, like the one tested during the SolAir 200 experimental campaign (T  lez, 2003), whose dimensions are defined in Section 3 together with the properties of the absorber material.

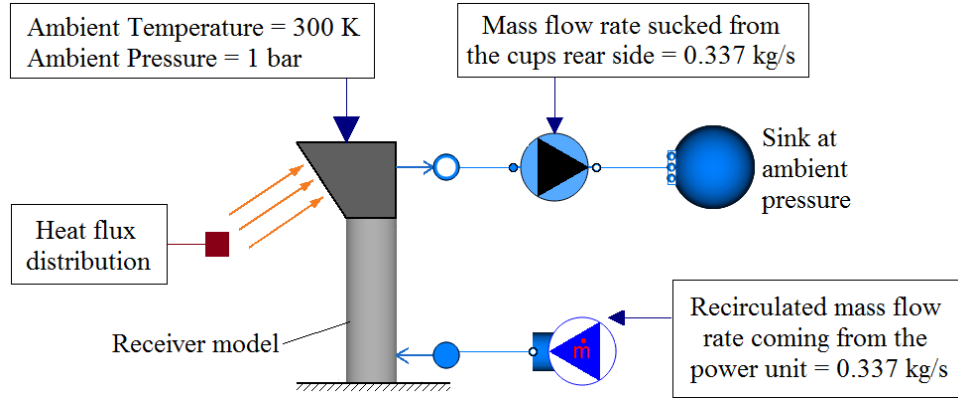


Figure 16 – Full receiver simulation environment developed in Modelica with the boundary conditions applied.

In the simulations, the total mass flow rate sucked from the rear side of the receiver is set to about 0.337 kg/s, corresponding to an air inlet speed of 0.75 m/s (the middle value among the air speeds parametrically varied at the micro-scale). The entire mass flow rate passing through the cups is then recirculated, assuming that the air temperature of the recirculated flow (i.e. the temperature at the outlet of the power unit) corresponds to 393 K, which is the nominal value at the J  lich solar tower plant (Hoffschmidt, 2014). The ambient temperature is set equal to 300 K, while the ambient pressure is 1 bar. The convective heat transfer coefficient between the receiver front face and the ambient air (H_{ext} in Eq. 16) is set equal to 10 W/m²K according to (Ho and Iverson, 2014). Figure 16 illustrates the simulation environment and the applied boundary conditions; note that there is no heat exchanger downstream the receiver, but it is simply imposed the mass flow rate to be extracted from the receiver rear side. The depth of the absorber structure has been shortened to 50 mm, as stated in Section 4.2.3.

The number of volumes along the flow direction is set to 15. The reliability of the solution has been proved by means of a grid independence analysis, which showed a deviation of only $\approx 1\%$ with respect to the 100 CVs case in terms of both temperature of the air outflow and temperature of the solid absorber at the front face.

5.1 Analysis in steady-state conditions

A first study has been conducted considering a uniform heat flux distribution of about 400 kW/m² and parametrically varying the ARR between the nominal value (0.4 according to T  lez (2003)) and the upper limit, in which all the return air is actually recirculated in the cups (ARR = 1). The inlet temperature of the recirculated air is kept to the nominal value of 393 K, independently by the ARR. This assumption implies that the mass flow rate of the cooling fluid in the heat exchanger changes accordingly with the air temperature reached at the receiver outlet, which depends on the ARR.

The aim of this study is to assess the influence of the ARR on the receiver performance. For this purpose, we introduce the receiver efficiency defined as the ratio between the final useful effect and the solar power absorbed on the receiver, see Eq. 27. The useful effect corresponds to the thermal power extracted from the heat exchanger downstream the receiver (see Figure 13a), neglecting the heat losses along the air circuit.

$$\eta = \dot{m}(h_{out} - h_{return})/\phi_{abs} \quad (27)$$

Figure 17 shows the results of this analysis including also the case in which the air gap between the cups is replaced by a sealing and, consequently, there is no recirculated air that flows in the receiver. In this case, the cup borders are assumed adiabatic and the warm air at the outlet of the heat exchanger is simply released in the environment.

Figure 17a shows that the receiver performance obviously improves increasing the ARR, since for any ARR lower than 1 a share of heated return air is lost in the environment. Moreover, Figure 17a proves the performance benefit of recirculating the warm air coming from the heat exchanger; in fact, a higher efficiency is obtained with respect to the case without the return air. Despite the overall positive effect of the recirculation, the improvement of the efficiency

is partially compensated by the larger convective and radiative heat losses that occur from the receiver front face. In fact, the higher the ARR the hotter the receiver front face (see Figure 17a), as a consequence of the increased air inlet temperature, as visible in Figure 17b. The volumetric effect is achieved for any ARR; however, the magnitude of the volumetric effect is about 50 % higher in the case without the air recirculation. This is because the air return flow, entering from the receiver back side, cools down the rear side of the cups.

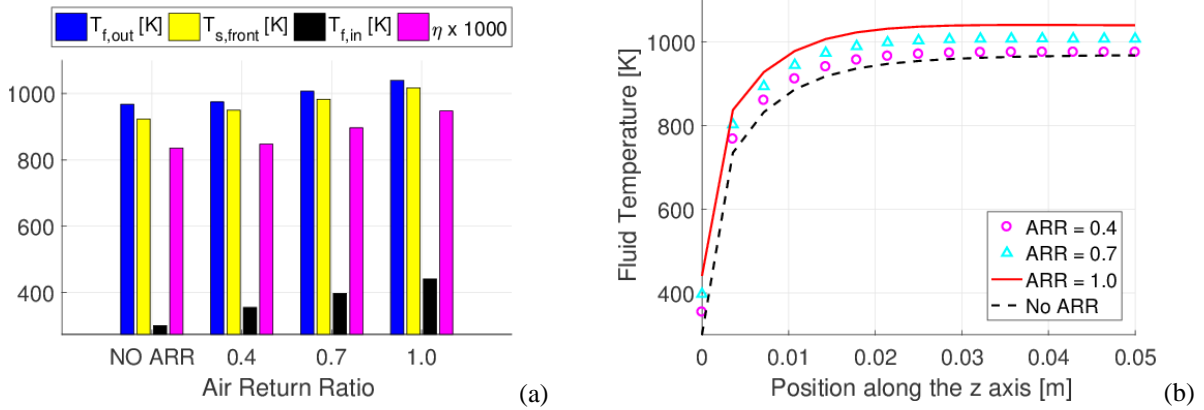


Figure 17 – (a) Key cup temperatures (air outflow $T_{f,out}$, inflow $T_{f,in}$ and solid front face $T_{s,front}$) plus the efficiency (multiplied by 1000) for different ARR, including the case without the return air (NO ARR). (b) Air temperature profile in the absorber along the flow direction for different ARR and without the return air.

After the case of uniform heat flux, a Gaussian distribution has been assumed to test the model under an unevenly distributed concentrated solar radiation, see Figure 18. The peak of the Gaussian is set to about 550 kW/m^2 while the standard deviation is imposed to be 0.4; with this setting, the average heat flux over the receiver surface is approximately the same of the previous section ($\approx 400 \text{ kW/m}^2$). In this analysis, the ARR is fixed to the nominal value of 0.4.

First, the receiver model has been simulated without acting on the orifices openings to regulate the mass flow rate distribution among the cups. Figure 19a and Figure 19b show the computed temperature at the receiver front face and mass flow rate cup by cup, respectively. As expected, the highest temperature is reached in the central cups where the heat flux is close to the peak value, while the mass flow rate is the lowest because of the density that decreases with the temperature. Without any orifices adjustment, the temperature difference among the cup front faces is remarkable ($> 1000 \text{ K}$).

To avoid the occurrence of high, and possibly dangerous, temperature peaks in the central cups, the mass flow rate can be regulated by cup acting on the orifices located at cups outlet, preserving the total value. This also allows increasing the peak flux incident on the receiver, leading to a benefit in terms of performance, since the occurrence of hot spots is prevented by the mass flow rate regulation. Moreover, avoiding very high local temperatures of the absorber structures helps limiting the radiative heat losses that depend on the fourth power of the temperature. The orifices should provide an additional pressure drop where a reduction of the coolant mass flow rate is required to increase the air outlet temperature. Therefore, the lower the heat flux, the higher the pressure drop caused by the orifice. For this reason, the imposed qualitative distribution of the pressure loss at the orifices corresponds to the incident heat flux map, which has been reversed in order to have the maximum value at the corner of the receiver and the minimum in the center. The latter is fixed to zero (no additional pressure adjustment is needed for the central cups); while the maximum value is changed iteratively until the pressure loss distribution that minimizes the temperature differences among the cups is found.

Imposing a maximum (additional) pressure loss of 21.5 Pa an almost uniform temperature of the receiver front face is achieved (about 37 K between the hottest and the coldest cup). The overall pressure drop across the receiver (porous medium plus orifices) increases by $\approx 70 \%$ with respect to the case without the orifices. Comparing Figure 19b and Figure 19c, it can be noticed that the mass flow rate now ranges in a shorter range of values and it is higher at the central cups in order to compensate the larger power incident on them.

The mass-flow-averaged air outlet temperature is about 870 K in the first case (no orifices adjustment) while it increases up to 974 K in the second case (almost homogenous receiver front face) as a consequence of the improved efficiency due to the absence of high temperature peaks.

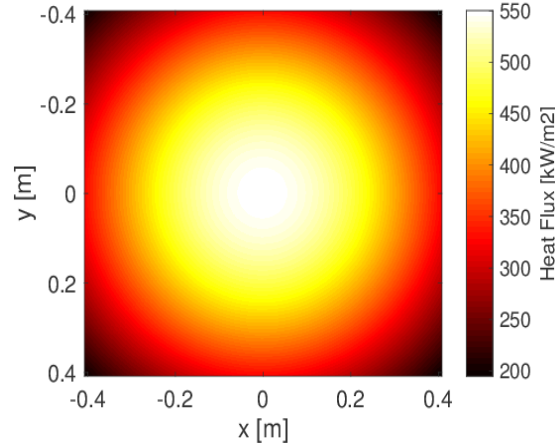


Figure 18 – Gaussian heat flux distribution imposed on the front face of the receiver

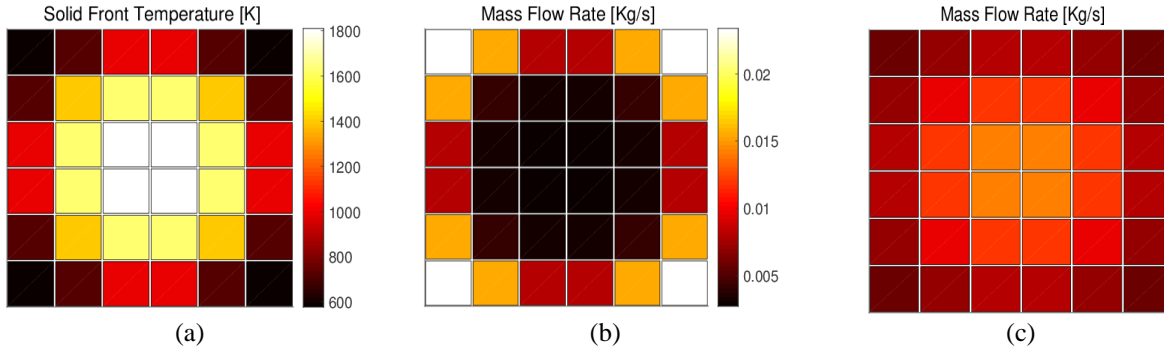


Figure 19 – Computed (a) front face temperature and (b) mass flow rate at the different 36 cups in the case of no orifice adjustment, and (c) mass flow rate distribution in the case adjusting the pressure drop at the orifices to homogenize the front face temperature

5.2 Analysis in transient conditions

The full receiver model can be exploited to simulate the receiver dynamic behavior under transient conditions, which are obviously of the greatest interest in the operation of a solar plant. Note that the present model is only able to predict the dynamic behavior of the absorber structure, the inertia linked with other pipes/manifolds behind the cups should be added depending on the specific receiver design as a separate model downstream the receiver. In this section, a first application of the full receiver model in transient conditions, without any additional inertia, is presented. The considered scenario consists of a fast passing cloud that instantaneously causes a drop of the incident solar radiation to zero, see Figure 20a. After the cloud passage, the simulation continues until the steady-state condition is reached again. The boundary conditions applied in this analysis are the same already considered in Figure 16 and a Gaussian distribution of the heat flux is imposed (see Figure 18), while the mass flow rate distribution among the cups is adjusted by means of the calibrated orifices as discussed in the previous section. The ARR is set to the nominal value equal to 0.4. This first dynamic analysis does not include the control system that regulating the mass flow rate keeps the air outlet temperature more or less constant; therefore, the mass flow rate sucked from the cups back side is always the same, according to Figure 16.

Figure 20b shows the evolution of the mass flow-averaged air outlet temperature during the transient, as well as the temperature of the solid structure at the front irradiated side and at the rear side of the cups.

The temperature of the solid front face sharply decreases by ≈ 300 K when the solar radiation is off, then, as soon as the thermal driver is restored, the temperature starts increasing and reaches the steady state value in about 3 minutes. This fast temperature variation, especially in the cooling phase, may cause critical stresses in the material, since a temperature rate of change higher than 150 K/min should be avoided (Smirnova et al., 2018); thus, a control strategy

has to be implemented. The prompt reaction of the receiver front face to a variation of the solar incident heat flux is because it is exposed to the external ambient; thus, the convective and radiative heat losses quickly cool down the receiver front face in the absence of the concentrated solar radiation. At the same time, if the receiver is irradiated, a large amount of the solar rays is absorbed very close to the front face (see Figure 4a); this explains the fast temperature increase when the cloud is passed. On the other hand, the temperature of the air at the receiver outlet and the one of the solid structure at the back side have a smoother behavior, which is obviously related to the thermal inertia (heat capacity) of the receiver.

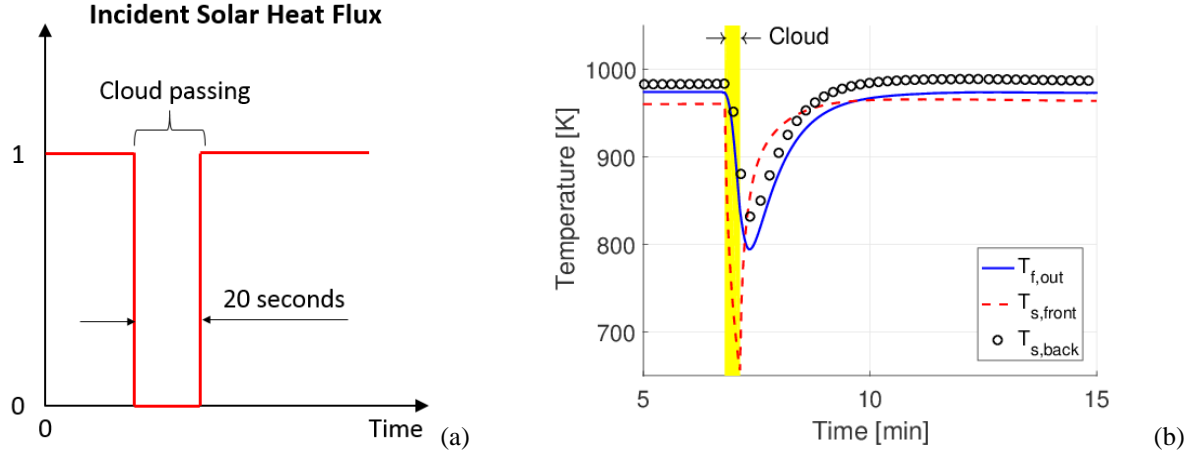


Figure 20 – (a) Incident solar heat flux multiplier, as a function of time. The cloud passage is simulated switching off the thermal driver for a given time interval. (b) Air outlet temperature ($T_{f,out}$) and solid temperature at the front irradiated side and at the back side ($T_{s,front}$ and $T_{s,back}$ respectively) during the transient. The time interval corresponding to the cloud passage is highlighted.

6 Conclusions

This paper presents a novel multiscale and modular approach applied to model an OVAR of the honeycomb-type. The receiver is numerically modeled scaling up the micro-scale model (single channel) to the macro-scale one (whole receiver), exploiting the results obtained at the micro-scale to characterize the thermal-hydraulic model of the meso-scale, which is finally used to modularly generate the macro-scale. The goal is to simulate the whole receiver with an acceptable computational cost while keeping the accuracy of the results as high as possible.

The full receiver model is modularly generated as a matrix of cups, which are thermally connected by means of the air gap that separates the adjacent cups, where the air stream coming from the power unit flows and removes the heat from the absorber modules. A preliminary comparison against the experimental data collected during the SolAir 200 tests campaign has been conducted, reproducing the experimental setup with the macro-scale model. Despite the differences between the model and the experiment, the outcomes of this comparison showed that the receiver model explains the experimental data for most of the simulated points. Then, the receiver model has been successfully simulated in order to assess the influence of the return air flow on the receiver performance at uniform heat flux, which, as expected, improves increasing the ARR. The receiver model has been also used, in the case of a non-uniform heat flux distribution, to calibrate the pressure drop given by the orifices at the cup rear side, with the aim of obtain an almost homogenous temperature of the receiver front face that allows avoiding high peak temperatures that lead to thermal stresses and high heat losses.

A transient scenario consisting in a fast passing cloud has been simulated considering a non-uniform heat flux distribution, with the orifices calibrated. The results show that, without any control strategy, the temperature of the receiver front face is very reactive to a variation of the incident solar radiation and it suddenly drops down if the solar heat flux is switched off.

As a perspective, the receiver model should include also the external air flow, which determines, for example, the actual convective heat transfer coefficient between the front frame and the environment, as well as the local value of the air return ratio. To this purpose, a CFD study should be carried out to characterize the external air flow influence on the receiver.

References

- Abbott, D., 2010. Keeping the energy debate clean: How do we supply the world's energy needs?, in: Proceedings of the IEEE. pp. 42–66. doi:10.1109/JPROC.2009.2035162
- Ahlbrink, N., Belhomme, B., Pitz-Paal, R., 2009. Modeling and Simulation of a Solar Tower Power Plant with Open Volumetric Air Receiver, in: Proceedings of the 7 International Modelica Conference Como, Italy. doi:10.3384/ecp09430048
- AL-Rjoub, A., Rebouta, L., Costa, P., Barradas, N.P., Alves, E., Ferreira, P.J., Abderrafi, K., Matilainen, A., Pischow, K., 2018. A design of selective solar absorber for high temperature applications. *Sol. Energy* 172, 177–183. doi:10.1016/j.solener.2018.04.052
- Ávila-Marín, A.L., 2011. Volumetric receivers in Solar Thermal Power Plants with Central Receiver System technology: A review. *Sol. Energy* 85, 891–910. doi:10.1016/j.solener.2011.02.002
- Blanco, M.J., Amieva, J.M., Mancilla, A., 2005. The Tonatuh Software Development Project: An open source approach to the simulation of solar concentrating systems, in: Proceedings of the ASME Computers and Information in Engineering Division. pp. 157–164. doi:10.1115/IMECE2005-81859
- Cagnoli, M., Savoldi, L., Zanino, R., Zaversky, F., 2017. Coupled optical and CFD parametric analysis of an open volumetric air receiver of honeycomb type for central tower CSP plants. *Sol. Energy* 155. doi:10.1016/j.solener.2017.06.038
- Capuano, R., Fend, T., Schwarzbözl, P., Smirnova, O., Stadler, H., Hoffschmidt, B., Pitz-Paal, R., 2016. Numerical models of advanced ceramic absorbers for volumetric solar receivers. *Renew. Sustain. Energy Rev.* doi:10.1016/j.rser.2015.12.068
- Capuano, R., Fend, T., Stadler, H., Hoffschmidt, B., Pitz-Paal, R., 2017. Optimized volumetric solar receiver: Thermal performance prediction and experimental validation. *Renew. Energy* 114, 556–566. doi:10.1016/j.renene.2017.07.071
- Du, S., He, Y.L., Yang, W.W., Liu, Z. Bin, 2018. Optimization method for the porous volumetric solar receiver coupling genetic algorithm and heat transfer analysis. *Int. J. Heat Mass Transf.* 122, 383–390. doi:10.1016/j.ijheatmasstransfer.2018.01.120
- FCT-Keramik, 2015. Silicon Carbide Material Specifications.
- Fend, T., Schwarzbözl, P., Smirnova, O., Schöllgen, D., Jakob, C., 2013. Numerical investigation of flow and heat transfer in a volumetric solar receiver. *Renew. Energy An Int. J.* 60, 655–661.
- Hennecke, K., Schwarzbözl, P., Koll, G., 2007. The solar tower Julich- A solar thermal power plant for test and demonstration of air receiver technology, in: Proceedings of ISES World Congress 2007: Solar Energy and Human Settlement. pp. 1749–1753. doi:10.1007/978-3-540-75997-3_358
- Hirsch, T., Ahlbrink, N., Pitz-Paal, R., Boura, C.T., Hoffschmidt, B., Gall, J., Abel, D., Nolte, V., Wirsum, M., Andersson, J., Diehl, M., 2011. Dynamic simulation of a solar tower system with open volumetric receiver - a review on the VICERP project, in: SolarPACES 2011 Conference Proceedings.
- Ho, C.K., Iverson, B.D., 2014. Review of high-temperature central receiver designs for concentrating solar power. *Renew. Sustain. Energy Rev.* 29, 835–846. doi:10.1016/j.rser.2013.08.099
- Ho, C.K., Mahoney, A.R., Ambrosini, A., Bencomo, M., Hall, A., Lambert, T.N., 2013. Characterization of Pyromark 2500 Paint for High-Temperature Solar Receivers. *J. Sol. Energy Eng.* 136, 014502. doi:10.1115/1.4024031
- Hoffschmidt, B., 2014. Receivers for Solar Tower Systems.
- Hoffschmidt, B., Téllez, F.M., Valverde, A., Fernández, J., Fernández, V., 2003. Performance Evaluation of the 200-kWth HiTRec-II Open Volumetric Air Receiver. *J. Sol. Energy Eng.* 125, 87–94. doi:10.1115/1.1530627
- Incropera, F.P., DeWitt, D.P., Bergman, T.L., Lavine, A.S., 2012. Fundamentals of Heat and Mass Transfer, sixth. ed, Wiley.
- IRENA, 2018. Renewable Power Generation Costs in 2017, International Renewable Energy Agency.
- Kribus, A., Gray, Y., Grijnevich, M., Mittelman, G., Mey-Cloutier, S., Caliot, C., 2014. The promise and challenge of solar volumetric absorbers. *Sol. Energy* 110, 463–481. doi:10.1016/j.solener.2014.09.035
- Marcos, M.J., Romero, M., Palero, S., 2004. Analysis of air return alternatives for CRS-type open volumetric receiver. *Energy* 29, 677–686. doi:10.1016/S0360-5442(03)00176-2
- Modelica Association, 2018. Modelica and the Modelica Association [WWW Document]. URL <https://www.modelica.org/> (accessed 2.7.18).
- Nield, D.A., Bejan, A., 1999. Convection in porous media, Convection in Porous Media. Springer, New York.
- Pang, X., 2017. High temperature solar selective absorber coating deposited by laser cladding. *Mater. Res. Express* 4.

doi:10.1088/2053-1591/aa8a7d

- Roldán, M.I., Fernández-Reche, J., Ballestrín, J., 2016. Computational fluid dynamics evaluation of the operating conditions for a volumetric receiver installed in a solar tower. *Energy* 94, 844–856. doi:10.1016/j.energy.2015.11.035
- Sani, E., Mercatelli, L., Jafrancesco, D., Sans, J.L., Sciti, D., 2012. Ultra-High Temperature Ceramics for solar receivers: spectral and high-temperature emittance characterization. *J. Eur. Opt. Soc.* 7, ISSN 1990-2573. doi:10.2971/jeos.2012.12052
- Smirnova, O., Fend, T., Capuano, R., Feckler, G., Schwarzbözl, P., Sutter, F., 2018. Determination of critical thermal loads in ceramic high concentration solar receivers. *Sol. Energy Mater. Sol. Cells* 176, 196–203. doi:10.1016/j.solmat.2017.11.033
- Smirnova, O., Fend, T., Schwarzbözl, P., Schöllgen, D., 2010. Homogeneous and Inhomogeneous Model for Flow and Heat Transfer in Porous Materials as High Temperature Solar Air Receivers, in: *Proceedings of the COMSOL Conference*. Paris.
- Stadler, H., Maldonado, D., Offergeld, M., Schwarzbözl, P., Trautner, J., 2019. CFD model for the performance estimation of open volumetric receivers and comparison with experimental data. *Sol. Energy* 177, 634–641. doi:10.1016/j.solener.2018.11.068
- Stadler, H., Tiddens, A., Schwarzbözl, P., Göhring, F., Baumann, T., Trautner, J., 2017. Improved performance of open volumetric receivers by employing an external air return system. *Sol. Energy* 155, 1157–1164. doi:10.1016/j.solener.2017.07.050
- Stobbe Tech A/S, 2017. SolAir projects [WWW Document]. URL <http://stobbe.com/research-projects/solar-energy/solair/> (accessed 1.13.17).
- Téllez, F.M., 2003. Thermal Performance Evaluation of the 200 kWh SolAir Volumetric Receiver, CIEMAT-PSA Technical Report (Report No. 1024). Madrid, Spain.
- Téllez, F.M., Romero, M., Heller, P., Ulmer, S., 2004. Thermal performance of SolAir 3000 kWh ceramic volumetric solar receiver, in: *12th International Symposium Solar Power and Chemical Energy Systems*. Oaxaca, Mexico.
- Teng, L., Xuan, Y., 2018. Thermal and hydrodynamic performance of a novel volumetric solar receiver. *Sol. Energy* 163, 177–188. doi:10.1016/j.solener.2018.01.087
- Wu, Z., Caliot, C., Flamant, G., Wang, Z., 2011a. Coupled radiation and flow modeling in ceramic foam volumetric solar air receivers. *Sol. Energy* 85, 2374–2385. doi:10.1016/j.solener.2011.06.030
- Wu, Z., Caliot, C., Flamant, G., Wang, Z., 2011b. Numerical simulation of convective heat transfer between air flow and ceramic foams to optimise volumetric solar air receiver performances. *Int. J. Heat Mass Transf.* 54, 1527–1537. doi:10.1016/j.ijheatmasstransfer.2010.11.037
- Yebra, L.J., Berenguel, M., Dormido, S., Romero, M., 2005. Modelling and simulation of Central Receiver Solar Thermal Power Plants, in: *Proceedings of the 44th IEEE Conference on Decision and Control, and the European Control Conference, CDC-ECC '05*. doi:10.1109/CDC.2005.1583357
- Zanino, R., Savoldi Richard, L., 2006. A review of thermal-hydraulic issues in ITER cable-in-conduit conductors. *Cryogenics (Guildf)*. 46, 541–555. doi:10.1016/j.cryogenics.2006.01.007
- Zhu, Q., Xuan, Y., 2017. Pore scale numerical simulation of heat transfer and flow in porous volumetric solar receivers. *Appl. Therm. Eng.* 120, 150–159. doi:10.1016/j.applthermaleng.2017.03.141